Accepted Manuscript

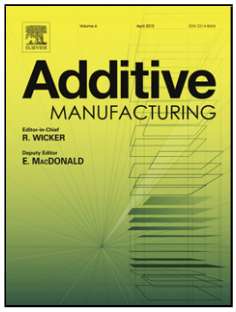

Title: Tailoring Green and Sintered Density of Pure Iron Parts using Binder Jetting Additive Manufacturing

Authors: Issa Rishmawi, Mehrnaz Salarian, Mihaela Vlasea

PII: S2214-8604(18)30473-1
DOI: https://doi.org/10.1016/j.addma.2018.10.015
Reference: ADDMA 538

To appear in:

Received date: 1-7-2018
Revised date: 21-9-2018
Accepted date: 5-10-2018

Please cite this article as: Rishmawi I, Salarian M, Vlasea M, Tailoring Green and Sintered Density of Pure Iron Parts using Binder Jetting Additive Manufacturing, *Additive Manufacturing* (2018), https://doi.org/10.1016/j.addma.2018.10.015

Tailoring Green and Sintered Density of Pure Iron Parts using Binder Jetting Additive Manufacturing

Issa Rishmawi[1], Mehrnaz Salarian[1], Mihaela Vlasea[1]

1-University of Waterloo, Department of Mechanical and Mechatronics Engineering, Waterloo, Ontario, Canada N2L 3G1

Submitted Electronically to: Journal of Additive Manufacturing

Note to Journal Editor:

Submission Date: **20 / 09 / 2018**

Number of Pages: **39**

Number of Figures: **14**

Number of Tables: **6**

Corresponding Author: Mehrnaz Salarian, PhD

Address: Department of Mechanical and Mechatronics Engineering, University of Waterloo, Waterloo, Ontario, N2L 3G1 Canada, e-mail: msalaria@uwaterloo.ca

Graphical abstract

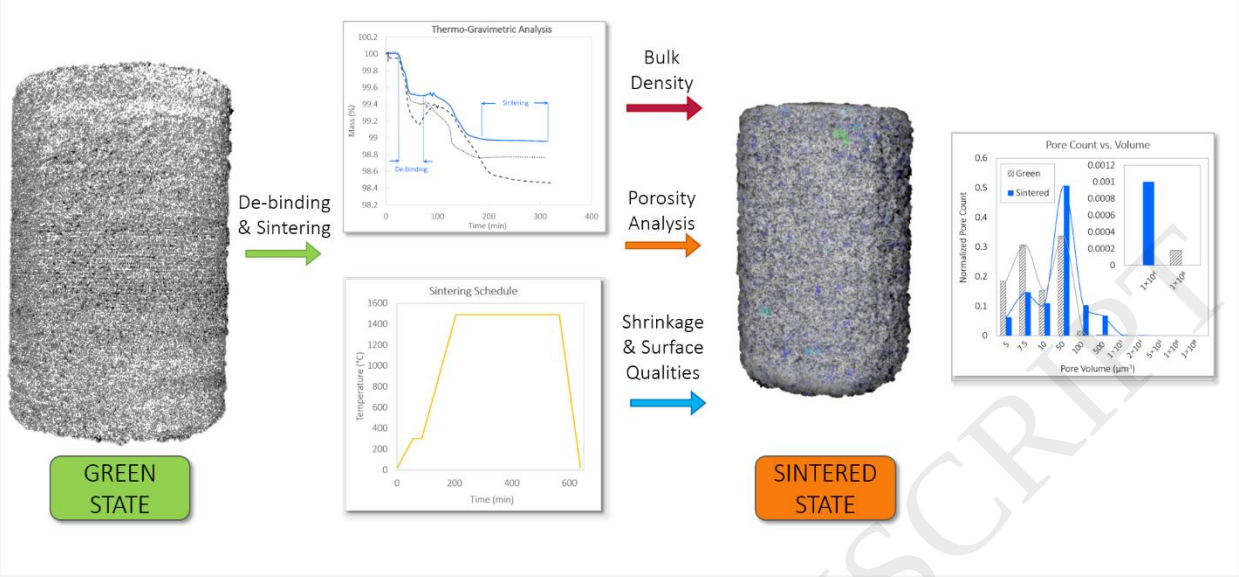

Abstract:

Binder jetting additive manufacturing (BJAM) is a comparatively low-cost process that enables manufacturing of complex and customizable metal parts. This process is applied to low-cost water-atomized iron powder with the goal of understanding the effects of printing parameters and sintering schedule on maximizing the green and sintered densities of manufactured samples respectively. The powder is characterized by using scanning electron microscopy (SEM) and particle size analysis (Camsizer X2). In the AM process, the effects of powder compaction, layer thickness and liquid binder level on green part density are investigated. Post-process heat treatment is applied to select samples, and suitable debinding parameters are studied by using thermo-gravimetric analysis (TGA). Sintering at various temperatures and durations results in densities of up to 91.3%. Image processing of x-ray computed tomography (μCT) scans of the samples reveals that porosity distribution is affected by powder spreading, and gradients in pore distribution in the sample are largely reduced after sintering. The resulting shrinkage ranges between $6.7 \pm 3.0\%$ and $25.3 \pm 2.8\%$, while surface roughness ranges between 11.6 ± 5.0 μm and 32.1 ± 3.4 μm. The results indicate that the sintering temperature and time might be tailored to achieve target densities anywhere in the range of 64% and 91%, with possibly higher densities by increasing sintering time.

Key words:

Binder jetting; additive manufacturing; irregular iron powder; sintering schedule; part density.

1 Introduction

Binder Jetting Additive Manufacturing (BJAM), also known as 3D Printing (3DP), is a powder bed additive manufacturing (AM) process, where the fabricated product is a "green" part that consists of the powder material adhered by the binder in a particular geometry, with generally low densities. Depending on the material system and final application, the green parts are infiltrated or sintered to impart the target functional material properties. Green parts are sintered in controlled conditions, which results in the burnout of all the binder and the formation of sinter necks between the powder particles, leading to a higher density part. BJAM of metals has been receiving lower

attention in comparison with other AM techniques, primarily because it results in comparatively lower part densities, in the range of 50 – 99% [1–9]. The BJAM technology has been used with a wide range of metals and alloys, such as iron or steel [2–5, 7, 10–24], titanium [6, 8, 25–31], nickel [9, 32–35], copper [1,15], lead [36,37], zirconium [38], zinc [39], gold [40] and magnetic neodymium-iron-boron [41], in addition to composite metal materials [42–45]. One major focus of BJAM applications for metals has typically been intentionally porous structures, such as biomedical implants [4,8,10,19,25,26,46]. Some of these applications have leveraged the special capabilities of BJAM, such as functionally graded properties [47–49]. Applications of BJAM with iron-based alloys include craniofacial bone implants [10], metal-ceramic-matrix materials for biomedical applications [44], hip and knee implants [4], as well as hot forging dies [11], injection molding tooling [12,13], and sound waveguides [14].

There are several advantages attributed to the BJAM technology, including scalability, ease of customization, minimal support structure requirements, and mitigation of residual stresses in parts due to the absence of high thermal gradients in metal sintering. One of the unique BJAM features is that it is an inherently inexpensive process, owing to its fast layer-by-layer manufacturing speed, low energy input to create geometries, and minimal environment atmospheric controls required to run the AM process. The costs are generally incurred in the secondary phase, when parts are sintered to fuse and consolidate the metal powder constituents and impart mechanical properties to the final part. To further leverage low-cost metal part production, it is useful to try to utilize the technology with inexpensive feedstock materials in order to maximize its economic potential. Exploiting this aspect of the technology can lead to increased industrial adoption. Water atomization is a much less expensive process used to produce metal powders than gas atomization. Schade et al. [50] compared water-atomized with gas-atomized powder characteristics as required for AM processes. The authors demonstrate that water-atomized powders are theoretically fit for use in AM processes. In general, water-atomization leads to an irregular particle shape, while gas atomization leads to a highly spherical shape. This is primarily attributed to the cooling rate the metal experiences. However, it is argued that a low water-to-metal ratio and a high water pressure can increase particle sphericity.

Typically, spherical powders allow for a higher packing density in the powder bed, thereby increasing the attainable density of a printed sample [9]. Inaekyan et al. [7] have utilized BJAM

with water-atomized iron powder and examined the densities and mechanical properties that can be obtained. The authors reported a green density nearing 40%, a sintered density of nearly 45% after sintering at 1100 °C for 2 hours and a volume shrinkage of nearly 8%. Further sintered densities of nearly 43% – 80% under various Hot Isostatic Pressing (HIP) or bronze infiltration regimes are reported. The low sintered density value (45%) is due to the low sintering temperature used, since the melting point of the iron powder is approximately 1538°C [51]. Densification through sintering is difficult to achieve at such low temperatures, since sinter neck formation is expected to be poor. However, the low temperature was deliberately selected in order to directly compare BJAM samples with those produced via Powder Metallurgy (PM) with similar sintering regimes. Mostafaei et al. [9] studied the microstructure and mechanical properties of BJAM samples made with water-atomized Inconel 625. The authors report a green density of near 50%. A maximum sintered density of 95% is achieved after sintering at 1270 °C for 4 hours, while a maximum shrinkage of 57% occurred after sintering at 1285 °C for 4 hours. Microstructural analysis shows that the samples contained pronounced precipitate formation and zones depleted of certain alloying elements, and tensile tests revealed comparatively low tensile strengths.

In general, the primary incentive for using water-atomized powder is its significantly lower cost compared to gas-atomized powders (the extent of cost reduction varies depending on suppliers), since water-atomization is currently the most common and economical means of producing metal powders [50]. Another possible incentive is that high-pressure water-atomization can lead to a higher yield of finer particles [50], which is useful for powder bed AM processes to increase packing density and part density [9].

In this study, the effects of BJAM in-process printing parameters and post-process sintering parameters on part density are studied with water-atomized iron powder. In-process, the effect of powder compaction on green part density is examined by the action of the rotating roller (powder spreader). The motion of a counter-rotating roller is typically shown to improve compaction and spreading of the powder, in contrast to a static spreader. To examine the extent of its impact on this powder, a comparison will be drawn between parts printed with the roller rotating and those printed with the roller in a static position. In addition, the effects of varying the layer thickness and liquid binder level on green part density are studied as well. Post-process, four sintering schedules are developed, and the effect of the heat treatment parameters on binder pyrolysis and final sample

density is studied. This study offers an analysis of the debinding and sintering schedule considerations for water-atomized iron powder in BJAM. Since water-atomized powders in AM typically produce lower powder packing density [50] and part density [9], studying the heat treatment considerations on part quality is helpful for understanding the potential of deploying water-atomized powders instead of gas-atomized powders at a significantly reduced feedstock cost. The approach derived in this study can serve as a starting point for more high-demand alloys such as steels. This is particularly useful for deploying BJAM in industry sectors currently relevant to PM, which are projected to be the first to benefit from disruptive adoption of the BJAM technology.

2 Materials and Methods

2.1 Material system

The powder material used is water-atomized pure iron powder (AT-1001-HP, Rio Tinto QMP, QC). The powder is sieved down to size < 45μm (USA Standard Test Sieve No. 325, Hogentogler & Co., Columbia, MD). The powder is characterized for size distribution (Retsch Camsizer X2, Newtown, PA) and surface morphology via scanning electron microscopy (SEM, LEO 1530, NY). The iron powder is blended with polyvinyl alcohol (PVA) powder (Alfa Aesar, Ward Hill, MA) with a particle size of < 63 μm, forming a blend of 99 wt% iron and 1 wt% PVA. Blending is performed by using a rotary tumbler (Thumler's A-R12, Auburn, WA) for 30 min. The PVA acts as a solid-state binding agent during the 3DP process. A water-based solvent (Zb^{TM} 60, Z Corporation, Burlington, MA) is used as a liquid-state binding agent. While the exact composition of the material is proprietary, the binder is an aqueous solution (approximately 85%-95% water) with some glycerol polymer content as the binding agent.

2.2 Additive manufacturing of samples

The 3DP process is conducted by using the above materials on the BJAM system ZPrint 310 Plus (3D Systems, Rock Hill, SC). In this study, three AM process variables are varied: roller actuation, layer thickness and liquid binder level. The roller actuation is varied from ON to OFF by manually disconnecting the roller pulley and taping the roller in place, thereby remaining static during printing. Layer thickness and liquid binder level are varied by changing the printing settings in the

machine. Cylindrical samples are printed, measuring 5 mm in diameter and 8 mm in height, with each printing batch containing 16 replicates. The build bed and feed bed have been modified from the original size using inserts to fit an *xyz* envelope of 32 × 32 × 50 mm^3 respectively. The experimental design levels for print parameters are summarized in Table 1. Liquid binder levels are presented in terms of saturation percentage per the machine setup – a value of 200% corresponds to a droplet size of 70 pL, and similarly, 300% to 105 pL.

2.3 Green samples density measurements

Initial estimations of the green density of the printed samples are first determined via geometrical and mass measurements. Geometrical measurements using calipers (Mitutoyo Absolute Digimatic Caliper, Mississauga, ON) and mass measurements using a scale (Sartorius Secura 225D, Göttingen, Germany) of the samples are performed, and the green density is estimated by using Equation (1), in which m is the mass of the sample, h is the sample height, and a and b are the major and minor diameters of the cylindrical samples. (The two different diameters are taken to reduce error in the measurement by avoiding the assumption of a uniform circular cross-section.)

$$\rho_{sample} = \frac{m}{\pi hab/4} \qquad (1)$$

Green densities are determined through x-ray computed tomography (μCT) (ZEISS Xradia 520 Versa 3D X-ray Microscope, Pleasanton, CA) by using the parameters in Table 2. The system provides a true spatial resolution of 700 nm with minimum achievable voxel size of 70 nm. Samples are stacked vertically in a sample holder. Cone beam X-rays illuminate the samples throughout the measurement. X-rays are transmitted through the samples, converted to photons in the visible light spectrum by a scintillator, magnified using an objective lens (4X), and finally detected by a charge-coupled detector (CCD). The sample is rotated over 360° while a sequence of two-dimensional images is taken. Once the scan is complete, reconstruction of the projection images is completed using ZEISS Scout-and-Scan™ Control System Reconstructor Software package, and a series of gray-scale images with 16-bit intensity ranges is produced.

Advanced image processing and porosity analysis are performed using Dragonfly Pro v3.1 (Object Research Systems Inc., Montréal, QC). The reconstructed dataset is denoised and filtered using the Non Local Means 3D filter. By using routine image processing steps such as grayscale

thresholding, the cropped dataset is segmented into the solid material and pores. Binarized images obtained following segmentation and morphological operations are used for relative density measurements. The binarized datasets are manually aligned with the Z axis of the μCT scanner corresponding to the build direction in ImageJ (Fiji, version 1.51) by using the "Rotate" function with bilinear interpolation. Relative density shows the distribution of porosity through the part, and is calculated by dividing 2D projections of the binarized porous dataset by a binary mask in which each pore is closed using the ImageJ plugin, "Fill Holes".

2.4 Debinding and sintering of samples

The framework for debinding and sintering can be developed based on previous work with this technology [6,7,9,52,53] and with similar materials [7]. The processes generally consist of three stages: curing (where water is evaporated from the samples by drying) at a comparatively low temperature, debinding (where the binder is removed) at medium temperature, and finally sintering at high temperature where densification occurs. There is typically a steady ramp up between the last two stages. The ramp up can be multi-staged where temperature is held for short intervals, which is typically not for metals [6,7,9], but for ceramics [52,53] in order to alleviate thermal stresses. This is the general approach taken in this study. Curing is performed by drying the samples in the build bed for a consistent duration at 40°C. Four post-process variables are studied: debinding temperature, debinding duration, sintering temperature and sintering duration. The rationale behind the selection of these parameters is described in depth in section 3.3. Debinding is performed under air starting from room temperature and ramping up at a rate of 5°C/min up to 250–350°C. The samples are kept at this temperature for 5–40 min, depending on liquid binder level and layer thickness, to facilitate burnout of the binder. To achieve sintering, the temperature is subsequently ramped up at 10°C/min up to 1390°C or 1490°C under 95%Ar–5%H_2 atmosphere and held for 2 hours or 6 hours. These temperatures correspond to 90% and 97% of the powder's melting point respectively. The temperature and duration of debinding are studied using thermo-gravimetric analysis (TGA) (Netzsch Jupiter STA 449 F1, Burlington, MA), which is presented in section 3.3. Sintering is performed by using the same TGA system (Netzsch Jupiter STA 449 F1, Burlington, MA). Inert Nitrogen gas is used as a protective gas in all heat treatment procedures. The TGA system is used for heat treatments instead of a curing oven and tube furnace in order to study mass change.

2.5 Sintered samples density measurements

Density analysis of the sintered sample is accomplished using μCT analysis, with a similar methodology as described for the green density analysis.

2.6 Sintered samples shrinkage measurements

The shrinkage incurred by the sintering process is quantified by using Equation (2), where x_G is the measured dimensional feature of a green sample and x_S is that of the sample after sintering. Shrinkage measurements were estimated in the radial and *z*-axis directions by using calipers (Mitutoyo Absolute Digimatic Caliper, Mississauga, ON).

$$Shrinkage\ in\ x = \frac{x_G - x_S}{x_G} \times 100\% \quad (2)$$

2.7 Uniaxial compression testing of sintered samples

For the purpose of this study, sintering is performed in a TGA system as opposed to a furnace, to study the effect of the sintering schedule on densification and mass change. As such, a limited yield of sintered samples could be reasonably produced. Uniaxial compression testing is performed on sintered samples as a preliminary test for mechanical properties. A uniaxial compression test system (MTS Criterion Model 43, Eden Prairie, MN) is utilized according to the ASTM E9 – 09 standard [54]. Samples are gently filed on the top and bottom surfaces to ensure flatness for the compression test. Testing is conducted at room temperature by using a 30-kN load cell at a strain rate of 0.001 s^{-1}. Three ($n = 3$) replicates of each sample are used for the compression test. In this study, the Weibull modulus described in Equation (3) is utilized as a means of quantifying the reproducibility of the sintered samples. Weibull moduli are typically used for brittle materials such as ceramics, or with ultimate tensile strengths in metals [55,56]. Since compression testing is performed in this study, yield strength is taken as the failure characteristic.

$$P(\sigma) = 1 - \exp\left[-\left(\frac{\sigma}{\sigma_0}\right)^m\right] \quad (3)$$

where P is the failure probability, σ is the measured stress, σ_0 is the scale parameter of the Weibull characteristic strength and m is the Weibull modulus. The probability of failure is calculated as described in Equation (4) [57], in which i is the measurement rank and n is the number of samples. The linearized form of the Weibull distribution is described in Equation (5).

$$P(\sigma) = 1 - \left(\frac{i-0.375}{n+0.4}\right) \quad (4)$$

$$ln(\sigma) = ln\left[ln\left(\frac{1}{P(\sigma)}\right)\right] \quad (5)$$

2.8 Surface roughness measurements

Surface roughness is characterized via laser confocal microscopy (Keyence VK-X250, Osaka, Japan). Image processing and measurements are completed by using the microscope scan processing software (Keyence VK-H1XME, Osaka, Japan). The roughness is measured in two locations: along the sides of the samples near the middle, and at the top of the samples near the center. The measurements are taken from approximately the same surface location on all samples for both side and top surface roughness. A scanning area of nearly 1400 × 1000 μm is taken in each surface scan, at a vertical *z*-axis resolution of 1 μm.

3 Results and Discussion

3.1 Powder characterization

The powder size distribution is determined to be 18 – 54 μm with a D_{50} of 34.1 ± 0.5 μm. The size distribution informed the selection of layer thickness levels in the study. Particle sphericity is found to be 0.9 – 0.75 for the size range, with larger particles showing decreasing sphericity. Sphericity at the D_{50} size is 0.8. Figure 1(a–b) illustrates SEM images of the powder, showing its irregular and angular shape.

3.2 Effect of AM process parameters on green density

The green densities are first estimated by dividing the measured masses of the samples by their caliper-measured volumes. The measured mass values are used to help threshold the μCT datasets associated with green parts in the image processing practice. The green densities of the samples are then obtained through further processing of μCT scans of the samples, as explained in section 2.3. The μCT-derived density values are summarized in Table 3. The highest green density obtained is 48.1% (sample set A, Table 1), with the roller actuated and with the lowest levels of layer thickness and liquid binder.

A visual representation of the green density results is presented in Figure 2(a–b) as a function of BJAM process parameters. The highest green density obtained is 48.1%, obtained at a layer thickness of 75 μm and a liquid binder level of 70 pL/drop. Based on the density values, it is seen that powder compaction through roller rotation plays an important role in increasing green density, warranting further studies on optimizing the roller rotational and translational velocity for this powder type. In addition, the results indicate that 75 μm layer thickness leads to higher green densities when the roller is actuated.

A lower layer thickness leads to a tighter powder packing in the bed, since the roller pushes down a thinner layer of particles onto the powder bed – in this case a thickness nearly twice the powder size [58]. In BJAM, a lower layer thickness also leads to a larger total volume of liquid binder deposited per unit of powder in the sample, since the liquid binder is jetted on a larger number of layers. The material system used in this study employed a solid powder binder, which is intended to dissolve when exposed to the liquid binder and thus create stronger adhesive bonds between metal particles in the green state. If an appropriate amount of binder is used, these bonding sites can promote sinter neck initiation during the metal sintering process [5,59].

A larger liquid binder volume can result in better dissolution of the solid state binder and stronger adhesive bonds between metal powder constituents. A balance must be reached in terms of the allowable ratio of binder constituents in the green state required to impart green part strength, and at the same time avoiding issues related to cracking and void formation during debinding and sintering, where binders are typically decomposed through pyrolysis.

The results in this study indicate that liquid binder level must be carefully controlled in order to increase green density. The results show that liquid binder-powder interaction is indeed complex, and there is an interplay of the powder compaction, layer thickness and liquid binder level process variables. Certainly a larger data set would be needed to study the interaction and to allow binder level optimization. The liquid binder occupies space in between the powder particles, therefore minimizing the binder level should increase density. However, too low of a binder level should be avoided, since an insufficient presence of the binder can lead to lack of adhesion and part crumbling. Having the binder level too high can cause layer shifting and lead to part geometry distortion. A larger study of liquid binder levels can be investigated as a future study for detecting

the threshold for maximizing green part density while avoiding green part crumbling. The range studied here is typical for the machine system used.

The total binder content in each sample set is calculated based on the liquid binder level and layer thickness. This is determined by multiplying the binder volume jetted in each layer by the number of layers. The print-head jets at 600 dpi (x,y), and the cross-sectional area of the samples in each layer is taken into account. The results are illustrated in Figure 3, and they reaffirm that liquid binder content has to be carefully controlled in correlation with the layer thickness, and other parameters of interest that may come into play and have not been considered in this study. This is shown in the shape of the distribution where the roller is activated, where the highest green density is obtained at the middle range. The deactivated roller samples suffer from spreading and compaction defects, and cannot be used to draw conclusions about total binder content. A wider selection of binder levels and layer thicknesses are useful for optimization and deeper conclusions.

The rotation of the roller has an impact on print quality. It is observed, during printing, that spreading of the powder is significantly less uniform when the roller is deactivated. Streaks of uneven spreading are noted, which is due to powder clinging to the static roller during spreading. In general, printing with the roller deactivated results in more noticeable layer shifting. This is reflected in the lower green densities obtained with the roller deactivated. The rotation of the roller results in a compaction force onto the powder. The powder particles are pushed closer together with each spread. The compaction of the powder layers is also beneficial in minimizing the seeping of the liquid binder outside the intended print area. This seeping out effect can be detrimental as it can lead to layer shifting. In fact, layer shifting is consistently observed in many of the samples printed with the deactivated roller rotation. It is also more noticeable with the higher liquid binder level of 105 pL/drop than with 70 pL/drop. No layer shifting is observed with any of the parts printed with the roller actuated.

3.3 Debinding analysis

As the green samples undergo heat treatment, the mixture of liquid binder and PVA constituents begins to disintegrate, leaving behind trace materials and pores. This process is known as “binder burnout” or pyrolysis [8]. Eventually, as the temperature elevates to just below the melting point of the metal, densification through sintering occurs, as sinter necks form and grow. Ideally, two

aspects of binder burnout must be ensured. First, complete binder pyrolysis should occur, such that no binder remains in the sample after debinding is complete. Second, oxidation of the metal should be avoided during debinding, as the binder disintegrates. Oxidation during debinding, specifically for iron, can impede densification during the sintering heat treatment, as well as impact phase changes, microstructure and mechanical performance. These two aspects can be tracked by monitoring the mass change in the sample during the debinding heat treatment through TGA. First, a test to determine the decomposition onset temperature of PVA alone is performed. Subsequently, the green samples are subjected to the complete heat treatment protocol to confirm a suitable debinding temperature, and if debinding time is an influential factor to consider for the debinding schedule. The suitability of the debinding temperature is judged by (1) suitable binder burnout, which would be evidenced by sample mass loss down to approximately 99% (in this case), and (2) minimal oxidation, which would be evidenced by minimal sample mass gain during debinding. However, understanding the full details of oxidation and pyrolysis products lies outside the scope of this test.

3.3.1 Pyrolysis of the binder material

Most of the binder by mass fraction present in the samples consists of PVA. On average, the PVA constitutes 0.98 ± 0.09 % of the green sample mass. The jetted liquid binder consists of mostly water, which is evaporated as the samples are dried, and glycerol. The glycerol completely decomposes between approximately 150°C and 230°C [60], which is below the debinding temperature threshold used in this study, and thus not considered critical. As such, TGA is conducted on the PVA alone in order to examine its decomposition temperature. The mass loss profile of the PVA binder is illustrated in Figure 4. This allows tracking of its thermal degradation behavior. Temperature is ramped up from ambient conditions to 600°C. It is evident that decomposition starts at nearly 270°C and continues until nearly 570°C, with rapid decomposition occurring between 270°C and roughly 360°C. These results are in agreement with PVA decomposition analysis in the literature [61]. Based on this analysis, 300°C is expected to be a suitable temperature for debinding of the green samples.

The burning process of the binder can result in complete and incomplete combustion products as well as the formation of various oxides. When sintering the printed samples, some of these

oxides could remain in the samples after debinding and only completely burn out before the onset of sintering.

Debinding analysis

Based on the pyrolysis analysis of the binder in the previous section, debinding is studied on the green samples (sample set A, Table 1) via TGA at 300°C, as well as 250°C and 350°C for comparison. In each case, the conditions of the heat treatment are kept constant as described in section 2.4 except for the debinding temperature. Samples are held at the respective temperature for 30 min. Figure 5 shows the mass change profiles of sample A undergoing the three heat treatments. The region of the first significant mass drop in the curves reveals differences between debinding at 300°C and 350°C. While the 300°C curve stabilizes after the drop, the 350°C curve displays a mass gain. This is taken as an indicator of significant oxidation of the metal taking place, which is not desirable. The second significant mass drop occurs as temperatures increase and sintering takes place. In this region, the curve of 300°C shows a steady drop in mass and a plateau at approximately 99% relative mass, which is an indication that the binder is largely burnt off. At 250°C, the PVA does not decompose readily as it is below the decomposition onset temperature shown in Figure 4. With this temperature, there is a higher chance of incomplete binder burnout. If incomplete burnout occurs, residual binder compounds may burn off as temperature increases prior to sintering, or in this case may lower the melting point of the iron powder because of the presence of carbon. Based on these observations, 300°C is taken to be a suitable temperature for debinding. Further studies on debinding via analytical techniques such as Fourier-transform spectroscopy (FTIR) can reveal the functional groups and exact chemistry of the compounds formed during pyrolysis.

Unlike temperature, the time of debinding is found to be dependent on process parameters. Three samples A, B, C (Table 1) are analyzed in this context according to the conditions described in section 2.4, with a debinding temperature of 300°C and variable debinding time and constant sintering temperature of 1390°C for 2 hours. Figure 6 illustrates the effect of layer thickness and liquid binder level on the required debinding time. Since the total number of layers affects the total volume of binder in the sample, the total binder volume is also considered.

For a given layer thickness, a higher binder level indicates that a larger volume of binder is jetted and hence requires a longer time for complete burnout. In Figure 6, comparing the curves A (70 pL/drop binder level) and B (105 pL/drop binder level) shows this trend. The total binder volume jetted in sample A is 82.1 μL, while in B it is 123.1 μL. Similarly, samples with a larger layer thickness have fewer layers than those with a smaller layer thickness – therefore they contain a smaller amount of binder and require a shorter time to completely burnout all the binder. This is reflected in the curves A (75 μm layer thickness) compared to C (100 μm layer thickness). Sample C takes a shorter time than A to burn out the binder since it contains only 61.4 μL of liquid binder, compared to the large volume contained in A. Overall, the results show that debinding time is an influential factor that should be considered to ensure a correct heat treatment, and that it is influenced by layer thickness and liquid binder level. It is therefore necessary to tailor the debinding process with special care to the BJAM process parameter selection, not just based on the material system constituents selected.

3.4 Sintering analysis

As the highest green density is obtained with sample set A (Table 1), sintering is performed on replicates of this sample set to analyze the final density after sintering for different sintering schedules. Sintered density is determined through μCT analysis, and is presented in Table 4.

The sintered density values indicate that obtaining high-density parts with water-atomized pure iron powder is possible, while maintaining shape fidelity. For the range of temperatures selected, sintered density increases with both higher sintering temperature and higher sintering time. A higher sintering temperature that is closer to the melting point of the powder, as well as a longer sintering duration can maximize the formation of sinter necks across the powder particles, thereby increasing the final density. The formation of sinter necks is driven by reduction of energy in the material system on a particulate level, which in turn depends on particle size [8]. The driving force behind sintering is dependent on crossing the activation energy barrier that promotes volumetric diffusion [8], such that keeping the system at one temperature for longer and longer durations will enable sintering until the total system energy is reduced to the minimum. In the temperature range for sintering studied here, volumetric diffusion is occurring as the activation energy for pure iron is in the range of 1000 – 1200°C [62]. Overall, these results indicate that tailoring of the final

density is possible by careful control of the sintering schedule. Increasing sintering time beyond 6 hours is expected to result in even higher densities based on the trend observed.

A parallel can be drawn between the work presented in this paper and that performed by Inaekyan et al. [7], as both use the same feedstock powder with the same technology to achieve a similar goal. In [7], the same water-atomized pure iron powder is used as in this work, but with a size distribution of 15 to 51 μm. The goal of that research is to investigate the viability of using water-atomized powders with BJAM technology. A commercial machine (ExOne M-Flex) is utilized in the study. Debinding is performed at 195 °C for 6 hours, which differs from the approach taken in this paper in that debinding is performed here at 300 °C for 5 – 40 min. In [7], sintering is completed under various conditions in Argon for 2 hours – including unassisted sintering at 1100 °C, bronze infiltration, and hot isostatic pressing (HIP) sintering at various temperatures and pressures. To provide a fair comparison, this work's results are compared to those of [7] that are performed under unassisted sintering at 1100 °C in Argon for 2 hours. Densities reported in [7] are nearly 40% for green samples and nearly 45% for sintered samples. The results of this paper contrast with the results of [7], in that sintering is performed at much higher temperatures for longer durations, which results in final densities between 64.5% (1390°C, 2 hours) and 91.3% (1490°C, 6 hours). The differences in the results stem from the differences in the debinding and sintering schedules. In particular, debinding at 300 °C is experimentally observed by the authors to completely facilitate binder burnout, and a sintering temperature of 1490°C is much closer to the melting point of the pure iron powder, and thus allows for more effective sintering. Furthermore, sintering under a 95%Ar – 5%H_2 environment mitigates the formation of a metal oxide layer in the samples. The hydrogen acts as a reducing agent as it strips any oxide layer that is formed, thereby improving the formation of sinter necks among iron particles. Furthermore, the duration of sintering greatly enhances the total energy absorbed by metal particles during sintering, as the 6-hour sintering leads to large increases in density in both temperatures.

This research provides an examination of the possible part densities that can be achieved with water-atomized iron powder in a BJAM system. Ultimately, the creation of a Master Sinter Curve (MSC) [8] is necessary in order to establish a robust framework that allows reliable and predictive tailoring of part densities based on established heat treatment regimes. The MSC would enable the selection of appropriate sintering schedules that can achieve high densities relevant to metal part

production (>90%) at lower temperatures than the temperature presented in this work (1490 °C), at the expense of higher time required to sinter components. Lower temperature furnaces with environment gas control are more economical, and generally preferred by industry.

3.5 Relative density, spatial porosity and pore shape analysis

A consistent voxel size for both green and sintered part scans is ensured to enable performing the same μCT analysis both before and after sintering. Due to the voxel size at which the parts are scanned, features with diameter below 16.5 μm cannot be reliably resolved. However, it has been reported that small size pores with negligible volumes have no significant impact on macro-level properties such as density [63]. For this study, 5.5 μm is deemed to be a reasonable voxel size in which μCT scanning of the part is completed in approximately 5-6 hours.

In general, thresholding values for segmentation are manually established by examining images prior to and after imposing the threshold to show the best contrast. Manual determination of the threshold values is not found to be practicable for green parts due to the small powder particle size of iron powder, high particle density, and interconnection of pore networks. Therefore, for the green parts, segmentation of the images is completed by using the estimated sample masses and material density. Based on the known density value of the iron powder (7.752 g/cm^3), the segmented sample volumes are multiplied by this density value to obtain the sample mass. The mass is assumed to be 99% iron for the green parts. For the sintered parts, the lack of interconnection seen in the pore network simplifies the analysis. As a result, thresholding values can be manually established by inspecting images before and after thresholding.

The filtered grayscale dataset is also resliced to an orthogonal view that can be flattened by using the Minimum Intensity Projection (MinIP) method to visualize the distribution of low density regions in the sample, and visually aligned with the relative density data in Figure 7(a-f). MinIP projects the voxel with the lowest attenuation value onto a single 2D image for the entire data set. It is assumed that PVA and liquid binder are not visible in any of the grayscale images owing to their significantly lower attenuation value. Therefore, they do not contribute to the size of the segmented section of the green parts. Slice-wise relative density calculation of the sample (sample set A, Table 1) before and after sintering is shown in Figure 7(a–f).

The relative density profiles of the green and sintered (1490°C, 6 hours) samples are shown in Figure 7(a), and they reveal the porosity distribution in the build direction (*z*-axis). In the green sample, porosity distribution shows variation in the build direction. In general, the large variation of relative density throughout the green sample is attributed to the BJAM process itself with a more in-depth analysis offered in prior work [8]. There is a periodicity of density variation, which can be seen as vertical bands in Figure 7(b) and (e), with the bands being almost equivalent to the layer thickness. In the regions of high variability (Figure 7(a) along the *z*-axis: 1347 μm to 2320 μm, and 3926 μm to 4921 μm shown also in Figure 7(d)), the bands correspond to a periodicity of 75.7 ± 5.7 μm, which reflects the layer thickness. This suggests that particle packing across a layer is tighter than in between layers. The high variation is mostly absent in the sintered samples, which is reflected in the absence of the vertical bands in Figure 7(c) and (f).

The overall lower regions (along the *z*-axis) of the green sample exhibit higher local densities approaching 65%, while in the central regions local density varies between approximately 40% and 55%. At the top of the sample, local density is at its lowest value. This trend is indicative of a powder compaction effect, either due to the roller or gravity. The repeated motion of the spreader in the AM system compacts the powder bed; topmost layers receive less compaction, resulting in reduced local density. Such effects, as well as the periodicity described above, are largely absent after sintering to 91.3% density. This is due to the fact that the sample is sintered at a high enough temperature, where such effects are essentially dampened by aggressive sintering and densification. To some extent, pore distribution is least concentrated near the central region of the sintered sample. A large collection of pores near the bottom of the sintered sample indicate a defect or a crack, shown by the dark "gash" in Figure 7(c) and the drop in local density in Figure 7(a).

Porosity also varies in the layer-wise (radial) direction, and this suggests a build orientation effect. In the green sample, a larger pore distribution is present at one side of the sample (top of Figure 7(b)). Specifically, powder spreading can lead to preferential packing of the build bed, where powder packing density varies in the bed during the AM process itself. This pattern is

echoed to some extent in the sintered sample, but is reduced with high temperature sintering and densification. This phenomenon is of interest and should be studied in more depth.

A comparison is also drawn across the four sintering schedules in terms of density profile. The density profiles are plotted in Figure 8. Variability in the density profile is observed in the cases of sintering at 1390°C, and to a much lesser extent at 1490°C. The profile of (1390°C, 2 hours) shows high variability in local density over small regions as well as over the entire sample height. This bears similarity to the green sample profile, except that local density is highest near the sample's center and lowest at the bottom. The profiles of (1390°C, 6 hours) and (1490°C, 2 hours) also show some variability in local density, which is attributed to periodic regions of poorer powder packing and thus poorer sinter neck formation. This trend is mostly not observed in the (1490°C, 6 hours) profile, where advanced sintering and densification overcome the effect of regions of poor powder packing.

The distribution of the number of pores is illustrated against pore volume in Figure 9(a) and against pore sphericity in Figure 9(b) for green and sintered (91.3% density) samples. Pore sphericity refers to the aspect ratio of the pores, where a value of 1 indicates a perfect sphere. The pore count is normalized against the total number of pores detected. The overall number of isolated pores is much higher in sintered samples than in green samples, but the pores are of lower volume (Figure 9(a–b)). Interconnected porosity is detected in the green samples, denoted by a pore volume greater than 1×10^{11} μm^3. It is not detected in the 91.3% density sintered samples, as pores become isolated after sintering to such a high density. In general, the distribution of pore volumes is narrower after sintering, particularly in the presence of interconnected porosity that dominates the volume (but not count) of pores in the green samples. Sphericity of the pores increases after sintering and approaches 1, with the majority of pores attaining values 0.6 and 0.7.

Three-dimensional render images from the μCT analysis of the sintered sample (1490°C, 6 hours) are presented, highlighting the distribution of pores by volume in Figure 10(a) and the distribution of pore sphericity in Figure 10(b).

3.6 Shrinkage analysis

The dimensional shrinkage of sample A (Table 1) is quantified by comparing the major and minor diameters *a* and *b* and height *h* before and after sintering. Maximum shrinkage occurred in the case of sintering at 1490°C for 6 hours, with a height shrinkage of 24.8 ± 3.5% and diametrical shrinkages of 25.3 ± 2.8% and 24.2 ± 2.1% respectively. A photographic representation of sample A in the green state and in the various states of sintering is shown in Figure 11(a–e7).

Shrinkage trends with respect to sintering temperature and time are illustrated in Figure 12(a–d). In general, larger shrinkage is associated with higher sintering temperature. Increasing the sintering temperature incurs much higher shrinkage (Figure 12(a–b)) than does increasing the sintering time (Figure 12(c–d)). No meaningful trend can be extracted from the shrinkage analysis about shrinkage in build direction (sample height *h*) compared to the horizontal direction (sample diameters *a* and *b*). A more expansive experimental design can be created with various sample geometries to reveal such trends, as they can reveal information about anisotropy or pore collapse in various directions. Other studies on BJAM of metals typically show shrinkage values of 2% – 32%, depending on powder, process and post-process parameters [1,6,7,13,19,24,25,27,28,40,64].

Radial uniformity in shrinkage is quantified by comparing shrinkage of the major and minor diameters. Shrinkage in the major and minor diameters vary by 5 – 33%, where sintering at 1490°C for 6 hours gives the best uniformity. Vertical uniformity in shrinkage is qualified by visual inspection of the samples. Shrinkage is generally uniform vertical direction for all sintering protocols, notwithstanding the dimensional accuracy of the AM process itself.

Consistency in shrinkage is assessed across multiple samples undergoing identical sintering protocols. This is quantified through the standard deviation in shrinkage (refer to Figure 12). The deviation is consistently low when sintering at 1390°C for 6 hours, which might suggest that sintering at a comparatively lower temperature for longer durations can boost consistency. Shrinkage is often an undesired outcome of densification through sintering. However, it can be compensated for if it is more or less consistent, such as in the case of sintering at 1390°C for 6 hours. Shrinkage can be accounted for through calculated dimensional compensation in the design

of a part. A more comprehensive experimental study can be designed to better assess shrinkage consistency in future research.

Mechanical properties

Uniaxial compression testing is performed on sintered samples. Weibull moduli and Young's moduli values are obtained from the results. The results are tabulated in Table 5. The highest yield strength obtained is 30.6 ± 15.8 MPa (1490°C, 2 hours), whereas the maximum Young's modulus obtained is 9.9 ± 0.3 GPa (1490°C, 6 hours). The Weibull moduli are low in comparison with typical metals [56], which reflects the high standard deviation in the yield strength values. Figure 13 shows the yield strength and Young's modulus plotted against density. Mechanical strength displays a trend with sample density. Samples at 79.1% density display higher Young's modulus than those with 84.0% density. However, the 79.1% density samples (1490°C, 2 hours) show a very high standard deviation in yield strength, which indicates that one of the measurement results is an outlier. Sintering in the TGA system limited the number of samples sintered for analysis, and further test could not be completed. The poor mechanical performance can be partially attributed to irregularly shaped pores in the samples (section 3.5), where larger pores can behave as notches (as in Figure 7(c)) that impact mechanical performance. Mechanical properties also depend on microstructure and grain size, which are influenced by the sintering conditions.

3.7 Surface roughness analysis

Surface roughness characterization is performed on the samples along the build direction (side surface) and perpendicular to the build direction (top surface). Surface correction for curvature is employed for scans along the side surface. The "arithmetical mean height" surface roughness metric S_a is utilized. The roughness values are summarized in Table 6. The lowest side surface roughness obtained corresponds to the samples sintered at 1490°C for 6 hours, with a value of 19.6 ± 3.4 μm. The lowest top surface roughness is 11.6 ± 5.0 μm, obtained at 1490°C for 2 hours.

Surface roughness improves significantly after sintering. Roughness drops by 8% – 29% after sintering at 1390°C and by 16% – 46% at 1490°C. Surface roughness measurements are plotted against density in Figure 14. Generally, sintering for a longer duration results in better surface finish in both cases of 1390°C and 1490°C. Sintering at higher temperatures for a fixed duration

also improves surface finish. In the green and all sintered states, top surfaces are smoother than side surfaces. This suggests a build orientation effect, where interlayer bonding or sintering results in rougher surfaces than across one layer. This might suggest that powder packing across one single layer is tighter than that in between layers due to the counter-rotating roller, resulting in superior sinter necking and thus better surface finish across the top layer.

Overall, BJAM process parameters and post-processing sintering parameters have a significant effect on final part qualities such as density, pore spatial distribution, pore morphology, pore interconnectivity, surface roughness, and mechanical characteristics. Depending on the application, an appropriate combination of process parameters and post-processing thermal treatment have to be carefully and holistically selected to achieve the target desired properties.

4 Conclusions

In this study, the effects of AM process parameters and post-process heat treatment on part density are studied on water-atomized pure iron samples printed with BJAM. The main findings are outlined as follows:

1. Density analysis through μCT scans reveals that green density is increased by minimizing layer thickness and carefully controlling liquid binder level. Liquid binder-powder interaction is complex and needs to be understood in further studies with larger datasets. Powder compaction in the bed allows for improved powder spreading and higher green densities, and optimization of powder spreading and compaction is of interest for future research. Overall, ranges of parameters wider than those included in this work can be studied for full exploration of the process map. Green densities of up to 48.1% are obtainable with water-atomized iron powder.
2. Optimization of the debinding process is a critical step to ensuring correct sintering. In this study, a suitable debinding temperature and duration are determined for the binder used, which results in complete binder burnout. However, complete binder burnout does not occur at the debinding temperature, Sintering can achieve densities of up to 91.3%.
3. This work demonstrates the viability of producing high density parts using water-atomized iron powder. Ultimately, an MSC is needed to enable complete tailoring of densities based on post-process heat treatment.

4. Pore distribution is affected by powder spreading. Green samples contain a higher pore concentration near the topmost regions and near one side of the sample, due to powder packing effects. The action of sintering reduces this trend. The density profile is reasonably consistent throughout the height of the sample.
5. The results obtained in this research might be used to tailor post-process heat treatment on BJAM parts in order to achieve a wide range of densities depending on target applications. Increasing the sintering time over 6 hours at temperatures nearing the melting point is expected to result in densities above 91.3%. Custom sintering schedules have to be developed for lower temperature furnaces to achieve appropriate densification.
6. Mechanical properties generally improve with higher sintering temperatures, due to more progressed sintering. A study that is more focused on mechanical characterization is needed for further analysis.
7. Shrinkage is drastically increased by increasing sintering temperature, and a more comprehensive study on consistency and uniformity in shrinkage might allow compensation for shrinkage by design.

Acknowledgments

This work was supported by funding from the Federal Economic Development Agency for Sothern Ontario (FedDev Ontario), in partnership with Rio Tinto. The authors would like to acknowledge the contribution of Rio Tinto for their support and mentorship throughout the completion of work. The authors also acknowledge the assistance of Dr. H. Asghari in SEM image procurement and Dr. E. Marzbanrad in TGA.

References

[1] Y. Bai, C.B. Williams, An exploration of binder jetting of copper, Rapid Prototyp. J. 21 (2015) 177–185. doi:10.1108/RPJ-12-2014-0180.

[2] Y. Tang, Y. Zhou, T. Hoff, M. Garon, Y.F. Zhao, Elastic modulus of 316 stainless steel lattice structure fabricated via binder jetting process, Mater. Sci. Technol. 32 (2016) 648–656. doi:10.1179/1743284715Y.0000000084.

[3] R. Frykholm, Y. Takeda, B.-G. Andersson, R. CarlströM, Solid State Sintered 3-D Printing Component by Using Inkjet (Binder) Method, J. Jpn. Soc. Powder Powder Metall. 63 (2016) 421–426. doi:10.2497/jjspm.63.421.

[4] M. Dourandish, D. Godlinski, A. Simchi, 3D Printing of Biocompatible PM-Materials, Mater. Sci. Forum. 534–536 (2007) 453–456. doi:10.4028/www.scientific.net/MSF.534-536.453.

[5] T. Do, C.S. Shin, D. Stetsko, G. VanConant, A. Vartanian, S. Pei, P. Kwon, Improving Structural Integrity with Boron-based Additives for 3D Printed 420 Stainless Steel, Procedia Manuf. 1 (2015) 263–272. doi:10.1016/j.promfg.2015.09.019.

[6] A. Basalah, Y. Shanjani, S. Esmaeili, E. Toyserkani, Characterizations of additive manufactured porous titanium implants, J. Biomed. Mater. Res. B Appl. Biomater. 100B (2012) 1970–1979. doi:10.1002/jbm.b.32764.

[7] K. Inaekyan, V. Paserin, I. Bailon-Poujol, V. Brailovski, Binder-jetting additive manufacturing with water atomized iron powders, APMI International Conference on Powder Metallurgy & Particulate Materials (2016).

[8] E. Wheat, Process Mapping and Optimization of Titanium Parts Made by Binder Jetting Additive Manufacturing, MASc thesis, University of Waterloo (2018).

[9] A. Mostafaei, J. Toman, E.L. Stevens, E.T. Hughes, Y.L. Krimer, M. Chmielus, Microstructural evolution and mechanical properties of differently heat-treated binder jet printed samples from gas- and water-atomized alloy 625 powders, Acta Mater. 124 (2017) 280–289. doi:10.1016/j.actamat.2016.11.021.

[10] D.-T. Chou, D. Wells, D. Hong, B. Lee, H. Kuhn, P.N. Kumta, Novel processing of iron–manganese alloy-based biomaterials by inkjet 3-D printing, Acta Biomater. 9 (2013) 8593–8603. doi:10.1016/j.actbio.2013.04.016.

[11] K. Agarwal, D. Mathur, R. Shivpuri, J. Lembo, Evaluation of ProMetal technique for application to dies for short run forgings, Solid Free. Fab Proc. Austin TX. (2002) 376–83.

[12] E. Sachs, E. Wylonis, S. Allen, M. Cima, H. Guo, Production of injection molding tooling with conformal cooling channels using the three dimensional printing process, Polym. Eng. Sci. 40 (2000) 1232–1247. doi:10.1002/pen.11251.

[13] S.M. Allen, E.M. Sachs, Three-dimensional printing of metal parts for tooling and other applications, Met. Mater. 6 (2000) 589–594. doi:10.1007/BF03028104.

[14] E.A. Rojas-Nastrucci, J. Nussbaum, T.M. Weller, N.B. Crane, Meshed rectangular waveguide for high power, low loss and reduced weight applications, in: IEEE, 2016: pp. 1–4. doi:10.1109/MWSYM.2016.7540079.

[15] A.C. Bailey, A. Merriman, A. Elliott, M.M. Basti, Preliminary Testing of Nanoparticle Effectiveness in Binder Jetting Applications, 27th Annual International Solid Freeform Fabrication Symposium (2016).

[16] H. Chen, Y.F. Zhao, Process parameters optimization for improving surface quality and manufacturing accuracy of binder jetting additive manufacturing process, Rapid Prototyp. J. 22 (2016) 527–538. doi:10.1108/RPJ-11-2014-0149.

[17] N.B. Crane, J. Wilkes, E. Sachs, S.M. Allen, Improving accuracy of powder- based SFF processes by metal deposition from a nanoparticle dispersion, Rapid Prototyp. J. 12 (2006) 266–274. doi:10.1108/13552540610707022.

[18] A. Elliott, S. AlSalihi, A.L. Merriman, M.M. Basti, Infiltration of Nanoparticles into Porous Binder Jet Printed Parts, Am. J. Eng. Appl. Sci. 9 (2016) 128–133. doi:10.3844/ajeassp.2016.128.133.

[19] D. Hong, D.-T. Chou, O.I. Velikokhatnyi, A. Roy, B. Lee, I. Swink, I. Issaev, H.A. Kuhn, P.N. Kumta, Binder-jetting 3D printing and alloy development of new biodegradable Fe-Mn-Ca/Mg alloys, Acta Biomater. 45 (2016) 375–386. doi:10.1016/j.actbio.2016.08.032.

[20] E. Sachs, M. Cima, J. Cornie, D. Brancazio, J. Bredt, A. Curodeau, T. Fan, S. Khanuja, A. Lauder, J. Lee, Three-dimensional printing: the physics and implications of additive manufacturing, CIRP Ann.-Manuf. Technol. 42 (1993) 257–260.

[21] C.B. Williams, J.K. Cochran, D.W. Rosen, Additive manufacturing of metallic cellular materials via three-dimensional printing, Int. J. Adv. Manuf. Technol. 53 (2011) 231–239. doi:10.1007/s00170-010-2812-2.

[22] H.J. Yoo, Reactive Binders for Metal Parts Produced By Three Dimensional Printing, Master's Thesis, MIT (1997).

[23] M. Ziaee, E.M. Tridas, N.B. Crane, Binder-Jet Printing of Fine Stainless Steel Powder with Varied Final Density, JOM. 69 (2017) 592–596. doi:10.1007/s11837-016-2177-6.

[24] D. Godlinski, S. Morvan, Steel Parts with Tailored Material Gradients by 3D-Printing Using Nano-Particulate Ink, Mater. Sci. Forum. 492–493 (2005) 679–684. doi:10.4028/www.scientific.net/MSF.492-493.679.

[25] A. Basalah, S. Esmaeili, E. Toyserkani, On the influence of sintering protocols and layer thickness on the physical and mechanical properties of additive manufactured titanium porous bio-structures, J. Mater. Process. Technol. 238 (2016) 341–351. doi:10.1016/j.jmatprotec.2016.07.037.

[26] F.E. Wiria, J.Y.M. Shyan, P.N. Lim, F.G.C. Wen, J.F. Yeo, T. Cao, Printing of Titanium implant prototype, Mater. Des. 31 (2010) S101–S105. doi:10.1016/j.matdes.2009.12.050.

[27] A. Basalah, S. Esmaeili, E. Toyserkani, Mechanical properties of additive-manufactured porous titanium bio-structures with oriented macro-scale channels, Int. J. Adv. Manuf. Technol. 84 (2016) 2239–2246. doi:10.1007/s00170-015-7849-9.

[28] S.M. Gaytan, M.A. Cadena, H. Karim, D. Delfin, Y. Lin, D. Espalin, E. MacDonald, R.B. Wicker, Fabrication of barium titanate by binder jetting additive manufacturing technology, Ceram. Int. 41 (2015) 6610–6619. doi:10.1016/j.ceramint.2015.01.108.

[29] J. Isaza, C. Aumund-Kopp, S. Wieland, F. Petzoldt, M. Bauschulte, D. Godlinski, New Materials and Applications by 3D-Printing for Innovative Approaches, Euro PM (2015).

[30] S. Maleksaeedi, J.K. Wang, A. El-Hajje, L. Harb, V. Guneta, Z. He, F.E. Wiria, C. Choong, A.J. Ruys, Toward 3D Printed Bioactive Titanium Scaffolds with Bimodal Pore Size Distribution for Bone Ingrowth, Procedia CIRP. 5 (2013) 158–163. doi:10.1016/j.procir.2013.01.032.

[31] F.E. Wiria, S. Maleksaeedi, Z. He, Manufacturing and characterization of porous titanium components, Prog. Cryst. Growth Charact. Mater. 60 (2014) 94–98. doi:10.1016/j.pcrysgrow.2014.09.001.

[32] A. Mostafaei, E.L. Stevens, E.T. Hughes, S.D. Biery, C. Hilla, M. Chmielus, Powder bed binder jet printed alloy 625: Densification, microstructure and mechanical properties, Mater. Des. 108 (2016) 126–135. doi:10.1016/j.matdes.2016.06.067.

[33] A. Mostafaei, Y. Behnamian, Y.L. Krimer, E.L. Stevens, J.L. Luo, M. Chmielus, Effect of solutionizing and aging on the microstructure and mechanical properties of powder bed binder jet printed nickel-based superalloy 625, Mater. Des. 111 (2016) 482–491. doi:10.1016/j.matdes.2016.08.083.

[34] P. Nandwana, A.M. Elliott, D. Siddel, A. Merriman, W.H. Peter, S.S. Babu, Powder bed binder jet 3D printing of Inconel 718: Densification, microstructural evolution and challenges☆, Curr. Opin. Solid State Mater. Sci. 21 (2017) 207–218. doi:10.1016/j.cossms.2016.12.002.

[35] M. Turker, D. Godlinski, F. Petzoldt, Effect of production parameters on the properties of IN 718 superalloy by three-dimensional printing, Mater. Charact. 59 (2008) 1728–1735. doi:10.1016/j.matchar.2008.03.017.

[36] J.P. Singh, R. Singh, Investigations for a statistically controlled rapid casting solution of lead alloys using three-dimensional printing, Proc. Inst. Mech. Eng. Part C J. Mech. Eng. Sci. 223 (2009) 2125–2134. doi:10.1243/09544062JMES1337.

[37] R. Singh, J.P. Singh, Comparison of rapid casting solutions for lead and brass alloys using three-dimensional printing, Proc. Inst. Mech. Eng. Part C J. Mech. Eng. Sci. 223 (2009) 2117–2123. doi:10.1243/09544062JMES1387.

[38] D.W. Lipke, Y. Zhang, Y. Liu, B.C. Church, K.H. Sandhage, Near net-shape/net-dimension ZrC/W-based composites with complex geometries via rapid prototyping and Displacive

Compensation of Porosity, J. Eur. Ceram. Soc. 30 (2010) 2265–2277. doi:10.1016/j.jeurceramsoc.2010.01.011.

[39] M. Kaplas, R. Singh, Experimental investigations for reducing wall thickness in zinc shell casting using three-dimensional printing, Proc. Inst. Mech. Eng. Part C J. Mech. Eng. Sci. 222 (2008) 2427–2431. doi:10.1243/09544062JMES1131.

[40] M. Lanzetta, M. Santochi, Liquid-phase Infiltration of Thermal Sintered Skeletons by Low-temperature Gold Eutectic Alloys, CIRP Ann. 55 (2006) 213–216. doi:10.1016/S0007-8506(07)60401-6.

[41] M.P. Paranthaman, C.S. Shafer, A.M. Elliott, D.H. Siddel, M.A. McGuire, R.M. Springfield, J. Martin, R. Fredette, J. Ormerod, Binder Jetting: A Novel NdFeB Bonded Magnet Fabrication Process, JOM. 68 (2016) 1978–1982. doi:10.1007/s11837-016-1883-4.

[42] J. Moon, A.C. Caballero, L. Hozer, Y.-M. Chiang, M.J. Cima, Fabrication of functionally graded reaction infiltrated SiC–Si composite by three-dimensional printing (3DP) process, Mater. Sci. Eng. A. 298 (2001) 110–119. doi:10.1016/S0921-5093(00)01282-X.

[43] U. Scheithauer, A. Bergner, E. Schwarzer, H.-J. Richter, T. Moritz, Studies on thermoplastic 3D printing of steel–zirconia composites, J. Mater. Res. 29 (2014) 1931–1940. doi:10.1557/jmr.2014.209.

[44] U. Scheithauer, Additive Manufacturing of Metal-Ceramic-Composites by Thermoplastic 3D-Printing (3DTP), (2015). doi:10.4416/JCST2014-00045.

[45] R. Soundararajan, G. Kuhn, R. Atisivan, S. Bose, A. Bandyopadhyay, Processing of Mullite-Aluminum Composites, J. Am. Ceram. Soc. 84 (2001) 509–513. doi:10.1111/j.1151-2916.2001.tb00691.x.

[46] J. Zhang, S. Zhao, Y. Zhu, Y. Huang, M. Zhu, C. Tao, C. Zhang, Three-dimensional printing of strontium-containing mesoporous bioactive glass scaffolds for bone regeneration, Acta Biomater. 10 (2014) 2269–2281. doi:10.1016/j.actbio.2014.01.001.

[47] A. Curodeau, E. Sachs, S. Caldarise, Design and fabrication of cast orthopedic implants with freeform surface textures from 3-D printed ceramic shell, J. Biomed. Mater. Res. 53 (2000) 525–535. doi:10.1002/1097-4636(200009)53:5<525::AID-JBM12>3.0.CO;2-1.

[48] M.C. Melican, M.C. Zimmerman, M.S. Dhillon, A.R. Ponnambalam, A. Curodeau, J.R. Parsons, Three-dimensional printing and porous metallic surfaces: A new orthopedic application, J. Biomed. Mater. Res. 55 (2001) 194–202. doi:10.1002/1097-4636(200105)55:2<194::AID-JBM1006>3.0.CO;2-K.

[49] A. Levy, A. Miriyev, A. Elliott, S.S. Babu, N. Frage, Additive manufacturing of complex-shaped graded TiC/steel composites, Mater. Des. 118 (2017) 198–203. doi:10.1016/j.matdes.2017.01.024.

[50] C.T. Schade, T.F. Murphy, C. Walton, Development of atomized powders for additive manufacturing, Powder Metallurgy Word Congress (2014).

[51] D. R. Askeland, P. P. Fulay, and W. J. Wright. The science and engineering of materials 6th edition, Cengage learning Inc (2010) pp. 889.

[52] M. Vlasea, R. Pilliar, E. Toyserkani, Control of structural and mechanical properties in bioceramic bone substitutes via additive manufacturing layer stacking orientation, Addit. Manuf. 6 (2015) 30–38. doi:10.1016/j.addma.2015.03.001.

[53] M. Vlasea, E. Toyserkani, R. Pilliar, Effect of Gray Scale Binder Levels on Additive Manufacturing of Porous Scaffolds with Heterogeneous Properties, Int. J. Appl. Ceram. Technol. 12 (2015) 62–70. doi:10.1111/ijac.12316.

[54] Standard Test Methods of Compression Testing of Metallic Materials at Room Temperature, ASTM E9 - 09, 2018

[55] S. Guo, R. Liu, X. Jiang, H. Zhang, D. Zhang, J. Wang, F. Pan, Statistical Analysis on the Mechanical Properties of Magnesium Alloys, Materials. 10 (2017) 1271. doi:10.3390/ma10111271.

[56] G. Straffelini, A. Molinari, Analysis of reliability of powder metallurgy steels by means of weibull statistics, Qual. Reliab. Eng. 8 (1992) 3–8. doi:10.1002/qre.4680080103.

[57] J. Absi, P. Fournier, J.C. Glandus, Influence of experimental parameters on the estimated value of Weibull's modulus, Journal of Materials Science 34.6 (1999) 1219-1227.

[58] S. Haeri, Y. Wang, O. Ghita, J. Sun, Discrete element simulation and experimental study of powder spreading process in additive manufacturing, Powder Technol. 306 (2017) 45–54. doi:10.1016/j.powtec.2016.11.002.

[59] R. Chumnanklang, T. Panyathanmaporn, K. Sitthiseripratip, J. Suwanprateeb, 3D printing of hydroxyapatite: Effect of binder concentration in pre-coated particle on part strength, Mater. Sci. Eng. C. 27 (2007) 914–921. doi:10.1016/j.msec.2006.11.004.

[60] B. Dou, V. Dupont, P.T. Williams, H. Chen, Y. Ding, Thermogravimetric kinetics of crude glycerol, Bioresour. Technol. 100 (2009) 2613–2620. doi:10.1016/j.biortech.2008.11.037.

[61] M. Vlasea, Additive Manufacturing Methodology and System for Fabrication of Porous Structures with Functionally Graded Properties, PhD thesis, University of Waterloo (2014).

[62] P. S. Liu, G. F. Chen, "Making porous metals" in Porous Materials: Processing and Applications, Elsevier (2014) 21 – 112. https://www.sciencedirect.com/science/article/pii/B9780124077881000022 (accessed June 26, 2018).

[63] M. Salarian, E. Toyserkani, The use of nano-computed tomography (nano-CT) in non-destructive testing of metallic parts made by laser powder-bed fusion additive manufacturing, Int. J. Adv. Manuf. Technol. 98 (2018) 3147–3153. doi:10.1007/s00170-018-2421-z.

[64] M. Dourandish, D. Godlinski, A. Simchi, V. Firouzdor, Sintering of biocompatible P/M Co–Cr–Mo alloy (F-75) for fabrication of porosity-graded composite structures, Mater. Sci. Eng. A. 472 (2008) 338–346. doi:10.1016/j.msea.2007.03.043.

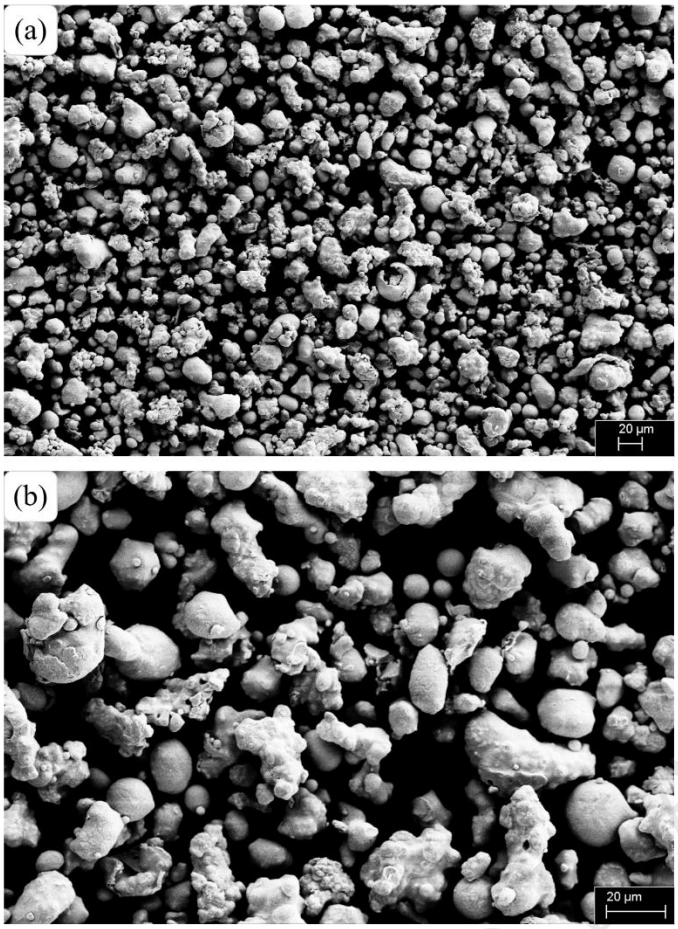

Figure 1 SEM images of the water atomized iron powder showing particle irregular morphology at magnifications of (a) 200× and (b) 500×

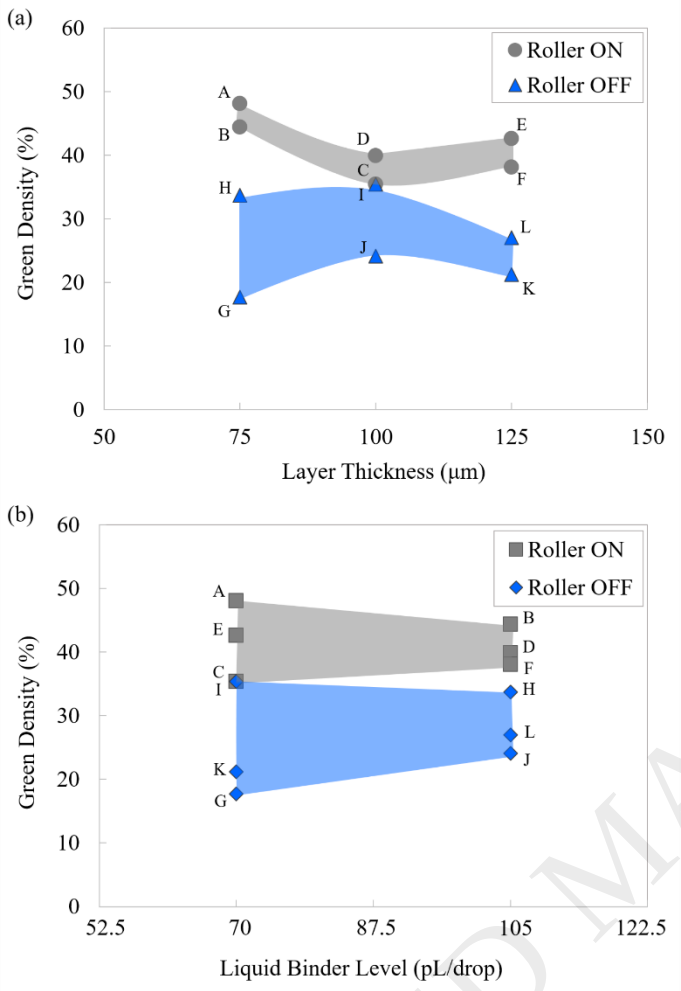

Figure 2 Plots of green density performance bands against (a) layer thickness and (b) liquid binder level. Sample set names are labelled. Trends show that with the roller actuated, green density increases with powder compaction.

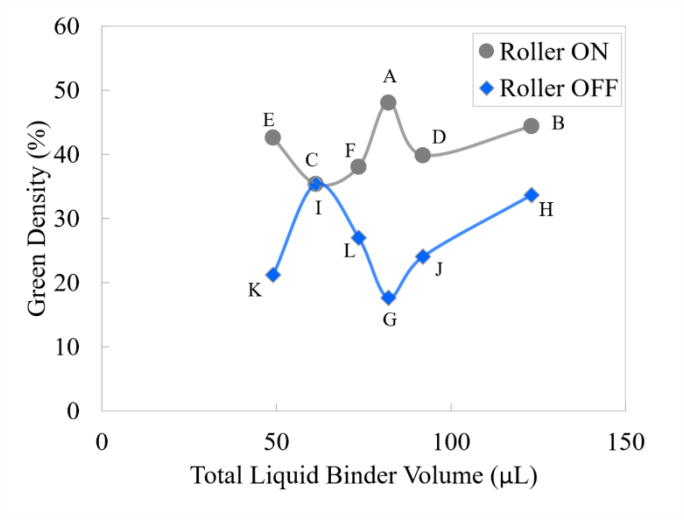

Figure 3 Green density against total binder volume in the samples, considering binder level and layer thickness. Highest density is achieved at the middle range of total binder content when the roller is activated (sample A).

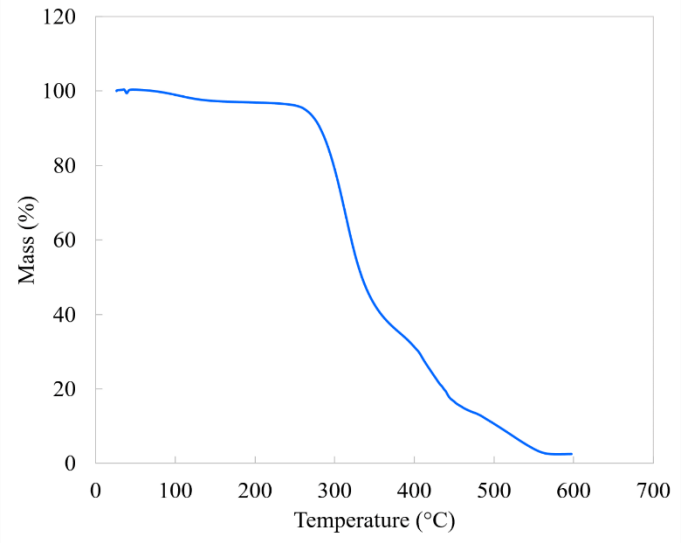

Figure 4 Mass loss profile of the PVA binder.

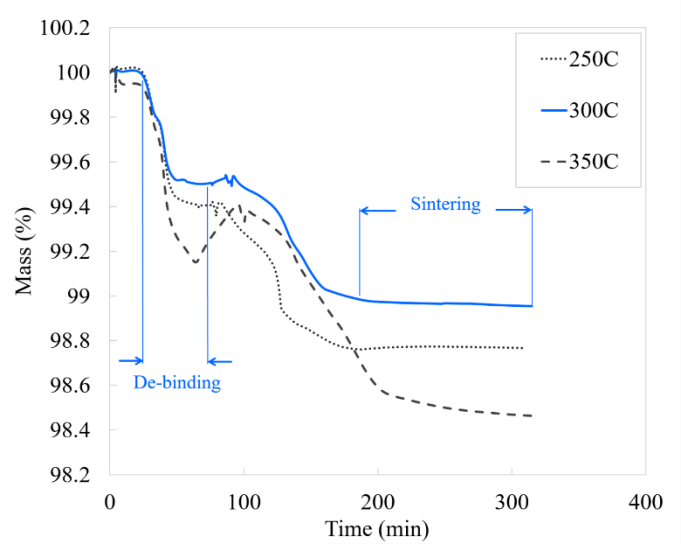

Figure 5 Mass loss of the green samples shows that 300 °C is a suitable debinding temperature. The regions of debinding and sintering are annotated for the 300°C curve.

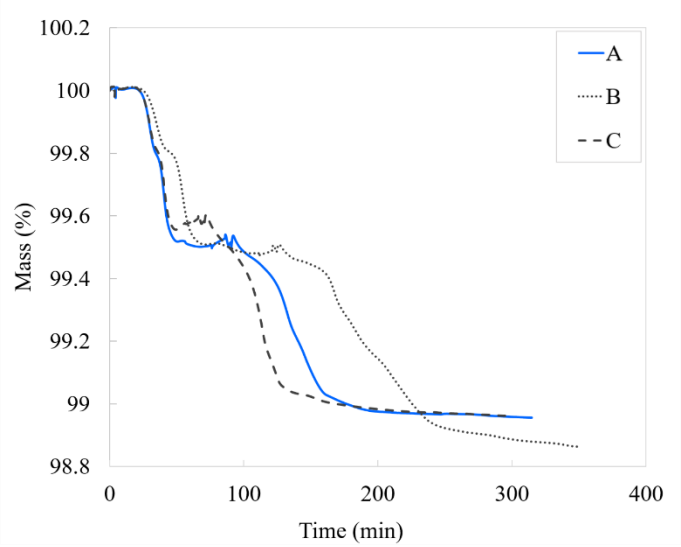

Figure 6 Effect of process parameters on debinding time. Comparing the curves of samples A and B shows that a higher binder level increases the time required for complete binder burnout; comparing the curves of samples A and C shows that a higher layer thickness decreases it.

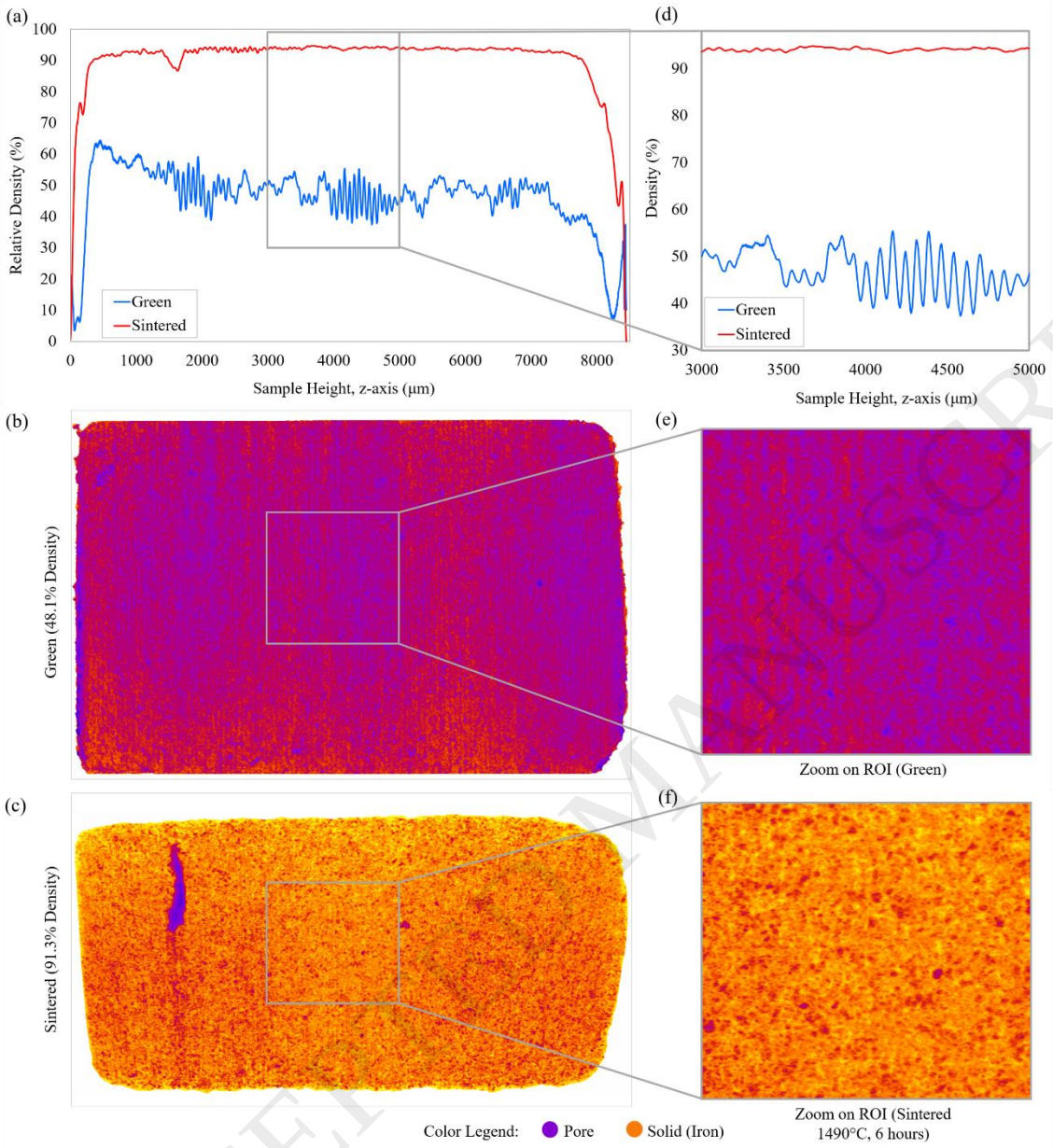

Figure 7 (a) Comparison of relative density profiles along sample height across green and sintered (1490°C, 6 hours) samples; (b) minimum intensity projection of the µCT scan showing pore distribution for the green and (c) sintered (1490°C, 6 hours) samples; (d) zoom on a region of interest (ROI) of the density profiles that is 2 mm in length; (e) minimum intensity projection of the µCT scan (zoom on a ROI) showing pore distribution for the green and (f) sintered (1490°C, 6 hours) samples. The sintered sample density profile and minimum intensity projection are rescaled in the *z* direction only.

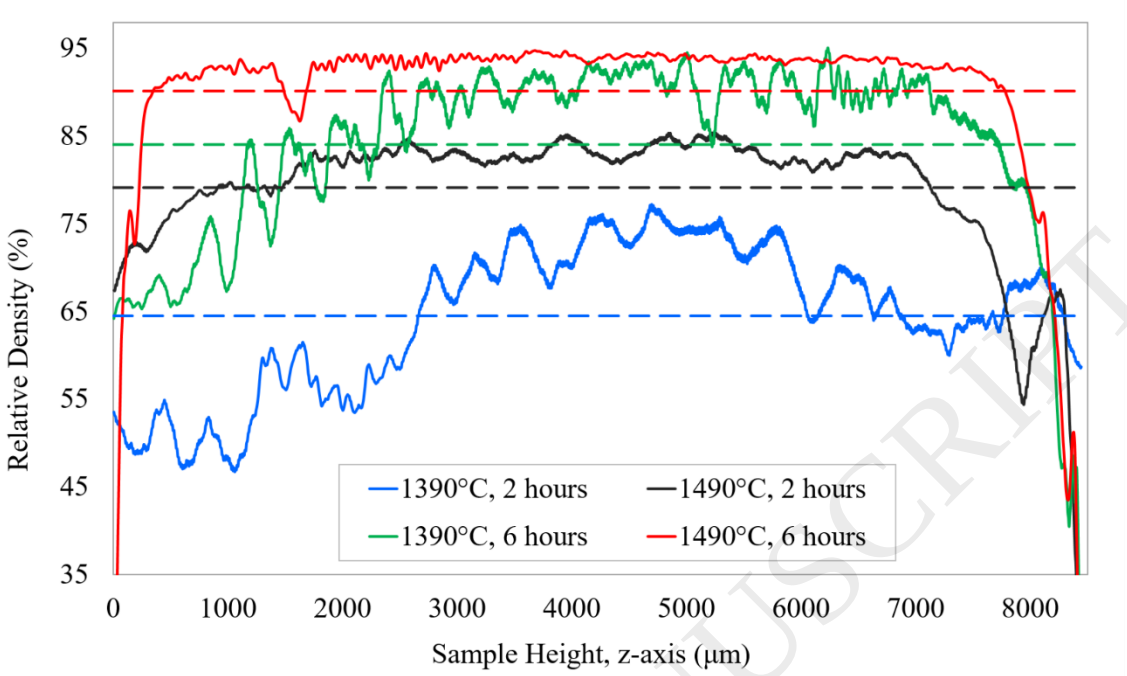

Figure 8 Relative density profile comparison across sintering schedules (average density value shown in dotted lines).

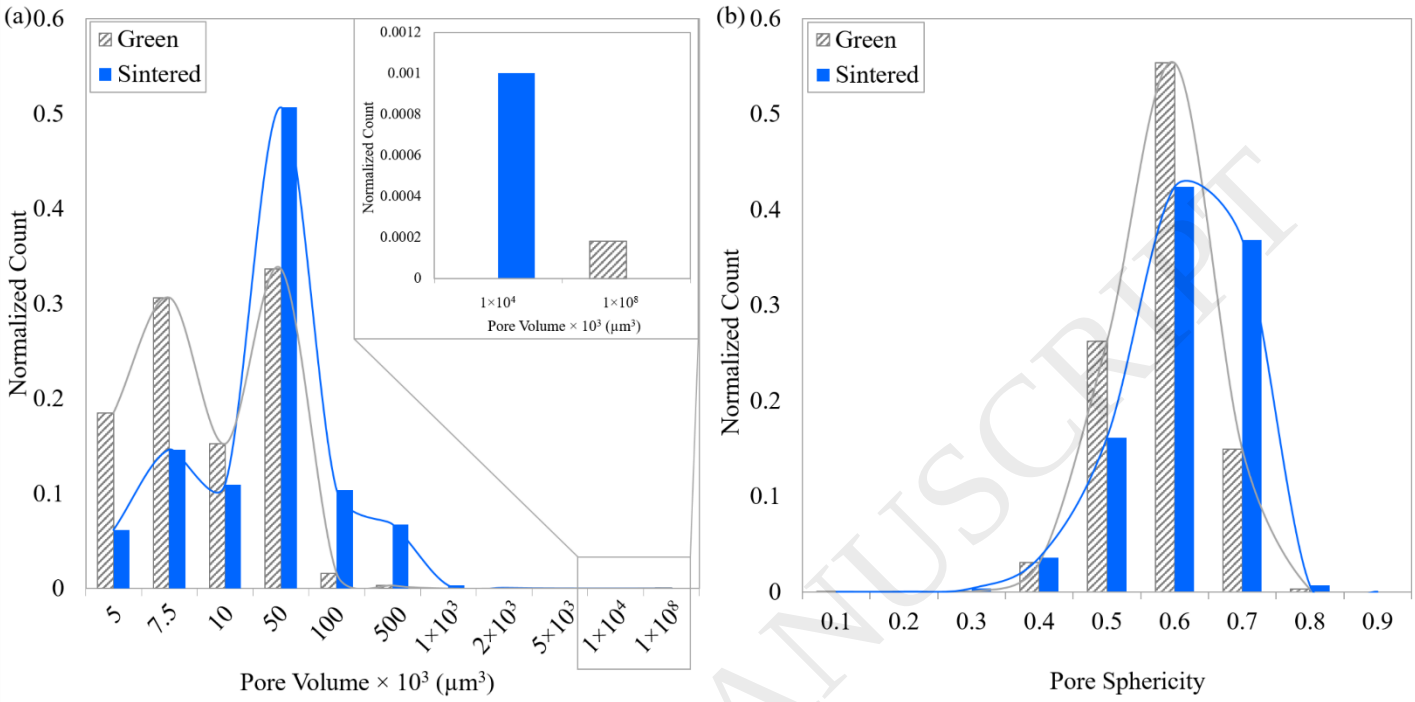

Figure 9 Histograms of pore count against (a) pore volume, and (b) pore sphericity for green and sintered (91.3% density), evaluated via µCT scan image processing. Pore volumes greater than 1×10^{11} µm^3 refer to an interconnected pore network that is detected only in the green samples.

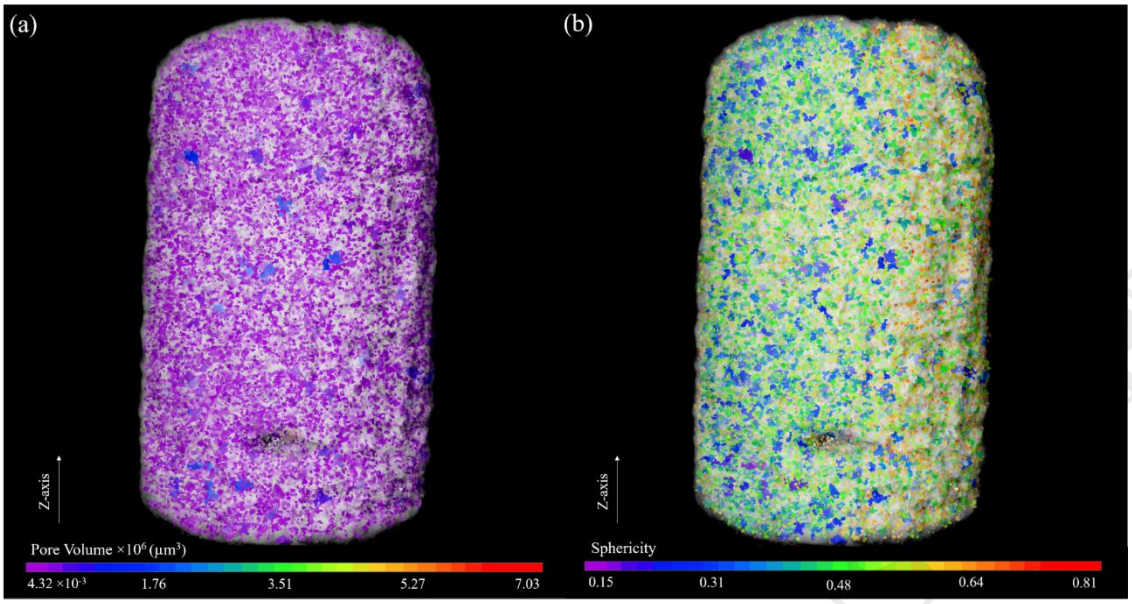

Figure 10 Three-dimensional rendering of μCT scans of a sintered sample (1490°C, 6 h) showing the distributions of (a) pore volume and (b) pore sphericity.

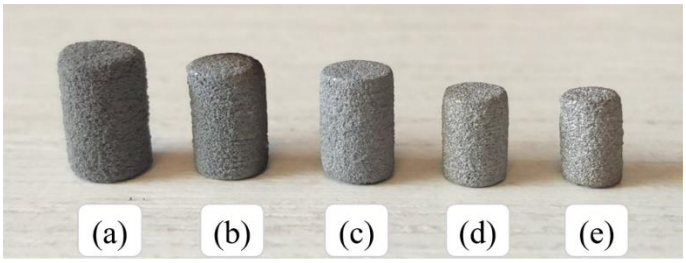

Figure 11 Dimensional shrinkage due to sintering. Sample A in (a) green state, and sintered at (b) 1390°C, 2 hours, (c) 1390°C, 6 hours, (d) 1490°C, 2 hours and (e) 1490°C, 6 hours. The extent of dimensional shrinkage correlates with density

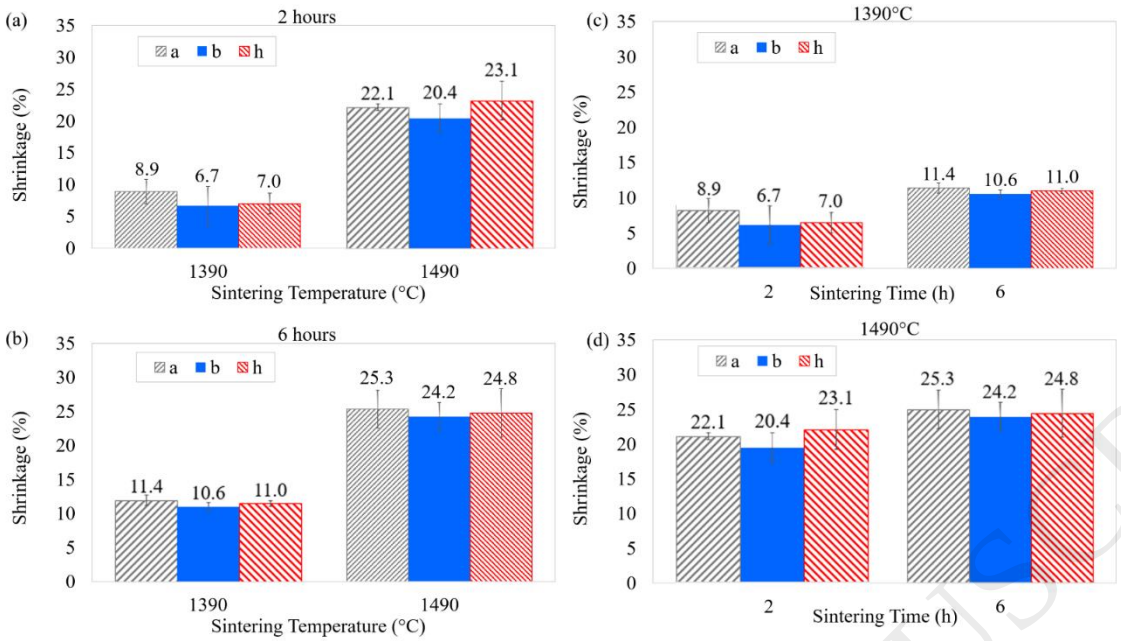

Figure 12 Shrinkage analysis shows that sintering temperature has a very drastic impact on shrinkage in both cases of (a) 2 hours and (b) 6 hours. Whereas sintering time has a slight effect on shrinkage in both cases of (c) 1390°C and (d) 1490°C. In this figure, *a* is the minimum cylinder diameter, *b* is the maximum cylinder diameter, and *h* is the cylinder height.

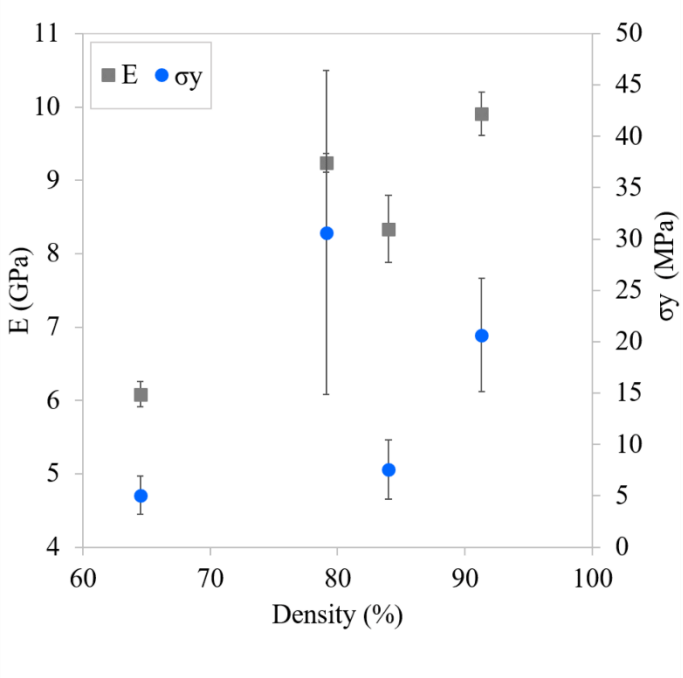

Figure 13 Plots of yield strength and Young's modulus against sample density; mechanical performance generally improves with higher sintering temperature due to more progressed sintering.

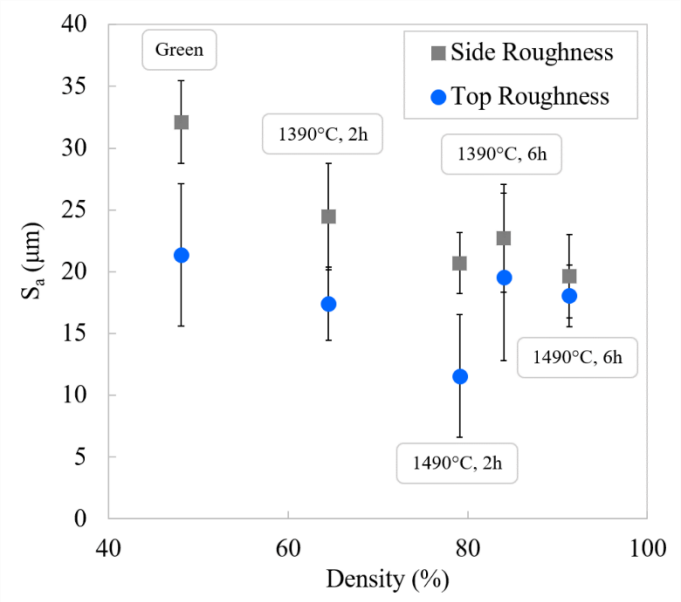

Figure 14 Higher densities generally result in smoother surfaces due to more progressed sintering. Top surfaces are smoother than side surfaces, suggesting a build orientation effect.

Table 1 The experimental design varies three variables: roller actuation, layer thickness and liquid binder level

Set Name	**Roller Actuation**	**Layer Thickness (μm)**	**Liquid Binder Level (pL/drop)***
A	ON	75	70
B	ON	75	105
C	ON	100	70
D	ON	100	105
E	ON	125	70
F	ON	125	105
G	OFF	75	70
H	OFF	75	105
I	OFF	100	70
J	OFF	100	105
K	OFF	125	70
L	OFF	125	105

**70 pL/drop ≡ 200%, 105 pL/drop ≡ 300% saturation level.*

Table 2 Parameters of μCT measurements

Parameters	
Source-to-detector distance (mm)	66.89
Voxel size (μm)	5.5
Voltage (kV)	140
Power (W)	10
Current (μA)	70
Source filter	HE2
Exposure time (s)	5.5
Optical magnification	4X
Camera binning	2
Number of projections	1201

Table 3 Green densities of printed samples determined via μCT analysis emphasize the effects of powder compaction, layer thickness and liquid binder level on print quality.

Set (Roller, Layer Thickness (μm), Liquid Binder Level (pL/drop))	**Green Density (%)**
A (ON, 75, 70)	48.1
B (ON, 75, 105)	44.4
C (ON, 100, 70)	35.4
D (ON, 100, 105)	39.9
E (ON, 125, 70)	42.6
F (ON, 125, 105)	38.1
G (OFF, 75, 70)	17.7
H (OFF, 75, 105)	33.7
I (OFF, 100, 70)	35.4
J (OFF, 100, 105)	24.1
K (OFF, 125, 70)	21.2
L (OFF, 125, 105)	27.0

Table 4 Sintered density values of the sample with the highest green density (sample A), under various sintering temperatures and durations.

Sintering Temperature (°C)	**Sintering Time (h)**	**Sintered Density (%)**
1390 (90% of T_m)	2	64.5
1390 (90% of T_m)	6	84.0
1490 (97% of T_m)	2	79.1
1490 (97% of T_m)	6	91.3

Table 5 Values of 0.2% offset yield strength, corresponding Weibull moduli and Young's moduli of the various samples, based on uniaxial compression testing.

Sintering Protocol	σ_y **(MPa)**	***m*** **(*R*²)**	***E*** **(GPa)**
1390°C, 2h	5.1 ± 1.8	2.60 (0.74)	6.1 ± 0.2
1390°C, 6h	7.5 ± 2.9	2.40 (0.69)	8.3 ± 0.5
1490°C, 2h	30.6 ± 15.8	1.95 (0.98)	9.2 ± 0.1
1490°C, 6h	20.6 ± 5.5	2.60 (0.50)	9.9 ± 0.3

Table 6 Average surface roughness results for side surfaces and top surfaces of sample A.

Sample	**Side Surface S_a (μm)**	**Top Surface S_a (μm)**
Green	32.1 ± 3.4	21.4 ± 5.7
Sintered 1390°C, 2h	24.5 ± 4.3	17.4 ± 3.0
Sintered 1390°C, 6h	22.7 ± 4.3	19.6 ± 6.8
Sintered 1490°C, 2h	20.7 ± 2.5	11.6 ± 5.0
Sintered 1490°C, 6h	19.6 ± 3.4	18.0 ± 2.5